Investigating the atomic level influencing factors of glass forming ability in NiAl and CuZr metallic glasses

Sina Sedighi, Donald Walter Kirk, Chandra Veer Singh,[a) and Steven John Thorpe
Department of Materials Science and Engineering, University of Toronto, Room 140, 184 College Street, Toronto, Ontario M5S 3E4, Canada

Bulk metallic glasses are a relatively new class of amorphous metal alloy which possess unique mechanical and magnetic properties. The specific concentrations and combinations of alloy elements needed to prevent crystallization during melt quenching remains poorly understood. A correlation between atomic properties that can explain some of the previously identified glass forming ability (GFA) anomalies of the NiAl and CuZr systems has been identified, with these findings likely extensible to other transition metal–transition metal and transition metal–metalloid (TM–M) alloy classes as a whole. In this work, molecular dynamics simulation methods are utilized to study thermodynamic, kinetic, and structural properties of equiatomic CuZr and NiAl metallic glasses in an attempt to further understand the underlying connections between glass forming ability, nature of atomic level bonding, short and medium range ordering, and the evolution of structure and relaxation properties in the disordered phase. The anomalous breakdown of the fragility parameter as a useful GFA indicator in TM–M alloy systems is addressed through an in-depth investigation of bulk stiffness properties and the evolution of (pseudo)Gruneisen parameters over the quench domain, with the efficacy of other common glass forming ability indicators similarly being analyzed through direct computation in respective CuZr and NiAl systems. Comparison of fractional liquid-crystal density differences in the two systems revealed 2-3 times higher values for the NiAl system, providing further support for its efficacy as a general purpose GFA indicator. © *2015 AIP Publishing LLC.* [http://dx.doi.org/10.1063/1.4931112]

I. INTRODUCTION

Bulk metallic glasses (BMGs) are now being used for a number of specialty device applications, with interest peaked by their unique set of mechanical and magnetic properties.[1–3] Unlike conventional crystalline alloys, bulk metallic glasses exhibit little to no long range atomic order, with structures essentially consisting of random, tightly packed clusters of atoms. The first experimental evidence of metallic glasses arose in 1959 when Klement, Willens, and Duwez were able to fabricate $Au_{75}Si_{25}$ metallic glass by splat quenching the metallic liquid melt onto a cold plate, resulting in rapid quenching at a rate of 10^5–10^6 K s^{-1} and thereby inhibiting crystallization.[4] While such methods provided a proof of concept, widespread application of amorphous metals on a consumer level was largely confined to thin films due to the kinetic demands of rapid heat transfer. As of today, a number of metallic glasses have been discovered which allow for fabrication methods involving far lower critical cooling rates,[5] and thus can be formed to much larger dimensions. These BMGs often share the common characteristics of being multi-component alloys, rich with transition metals (and noble metal-metalloid species) at or near deep eutectic compositions. Currently, a key focal point of BMG research is focused on the search and discovery of key parameters influencing glass forming ability (GFA), identifying how they are reflected in structural, ther-

modynamic, and kinetic properties and studying how these properties can be tuned in a controlled manner. Following these lines, many approaches have been proposed for the compositional tuning of BMGs;[6–12] however as of yet, a robust method capable of fine compositional tuning for the optimization of GFA in multicomponent alloys is ever elusive.

The high glass forming ability of zirconium-copper based multicomponent alloys makes the binary Cu–Zr system a prime focal point for analysis. Recently, independent studies investigating the compositional dependencies of glass forming ability in the Cu–Zr system have uncovered a number of influencing factors that inhibit crystal nucleation and growth.[13,14] The investigation of Li *et al.* of compositional dependencies of percent density changes (or excess free volume) upon crystallization $(\rho_c - \rho_{liq})/\rho_c$ showed direct correspondence with critical casting thicknesses, with experimental results indicating minimal density changes (minimal free volumes) for high GFA compositions of $Cu_{64}Zr_{36}$, $Cu_{56}Zr_{44}$, and $Cu_{50}Zr_{50}$. In accordance with free-volume theories for diffusive motion[15] and observed correlations between density change upon crystallization and viscosities at the liquidus/melting temperature,[11] these results suggest that enhanced atomic mobility constraints associated with more efficient liquid-state atomic packing in these select compositions are the root to their higher glass forming ability. Consistent with these notions, the experimental investigations of Russew *et al.*[16] into compositional dependencies of melt fragility in the CuZr alloy system found strong correlations with glass forming ability, with findings showing a clear minimum at the high GFA composition

---

a)Author to whom correspondence should be addressed. Electronic mail: chandraveer.singh@utoronto.ca

$Cu_{64}Zr_{36}$. On a parallel front, experimentally determined Turnbull coefficients and liquid-crystal interfacial energies, as well as molecular dynamics (MD) calculations of glass-glass interfacial energies were similarly successful in predicting trends in critical casting diameters in the Cu–Zr system.[14] With this in mind, Kang *et al.* proposed a nucleation barrier controlling nature dictating the glass forming ability of Cu–Zr alloys, with results of glass-glass interfacial energy calculations suggesting an underlying link to compositional and topological short-range ordering.[14]

Unlike CuZr, the Ni–Al system has recently been the focus of study due to its anomalously high crystallization rate for an equimolar binary alloy. While both systems possess similar atomic size ratios, similar atomic mobilities throughout the quench regime, and identical primary nucleating crystal phases (B2 phase), the equiatomic $Ni_{50}Al_{50}$ alloy possesses critical cooling rates orders of magnitude higher than $Cu_{50}Zr_{50}$, with crystal nucleation even being accessible under molecular dynamics time scales. The molecular dynamics investigation of Tang and Harrowell[17] of $Ni_{50}Al_{50}$'s anomalously high unidirectional crystal growth-rates in comparison to $Cu_{50}Zr_{50}$ uncovered striking differences in the extent of chemical ordering present at the liquid-crystal interface. Large amplitude and long length-scale density correlations extending well into NiAl's parent liquid phase were observed at the interface, while in contrast, correlations in the CuZr parent phase rapidly decayed away from the boundary, with little indication of induced ordering beyond a few atomic layers.[17] Understanding the underlying factors controlling the susceptibility for ordering at the interface may thus be key to understanding glass forming ability in general. It is likely that the differences observed are linked to more intrinsic differences in the nature of short-range chemical and topological ordering between the two systems. In support of these notions, recent analysis of glass pair-correlation functions for a number of different alloy systems has identified "hidden" topological differences between poor and ideal glass formers. It was found that scaled peak positions in the pair distribution function of glassy systems can roughly be decomposed into those corresponding to fcc or bcc crystal structures. Moreover, higher GFA alloys were found to exhibit a higher degree of intermixing between these corresponding fcc and bcc "hidden orders," suggesting that greater geometric frustration in these alloys inhibits crystallization.[18] While not discussed by Wu *et al.*,[18] a greater extent of topological entanglement of hidden orders and thus medium-range geometric frustration in the CuZr system may be a major constraining force on the degree and length scales of induced crystalline ordering at the interface. Furthermore, considering the similar compositional trends observed for interfacial free energies, extent of free volume, compositional/polytetrahedral short-range ordering, and compositional ordering at the interface, it is possible that a connection exists to some more fundamental underlying property at the bonding level. Currently, limited information is available regarding underlying bonding, short-range ordering, transport, and structural relaxation properties of the NiAl and CuZr amorphous phases, largely hindering the ability to concretely investigate such underlying connections.

Despite these significant advances, a clear-cut design approach for the compositional tuning of glass forming ability

in BMGs *a priori* has yet to be identified. Current computational and analytic tuning methods are severely limited in their applicability due to a number of non-trivial factors. For one, many of the identified GFA indicators and influencing factors (including the majority of those discussed above) are not single phase properties, often relating to properties of the disordered and crystallizing phases and/or the interface between the two. In complex multi-component systems, the equilibrium crystalline phase is rarely known before hand, with the crystallization pathway leading to the final equilibrium phase more often than not being a multi-step process involving several (also likely unknown) intermediate metastable phases. These considerations would then suggest the potential existence of severe limitations on the practicality of a computational (or experimental) method capable of rapid, accurate, and compositionally robust GFA tuning. Assuming an accurate inter-atomic potential is available, current molecular dynamics simulation methods readily allow for the sampling of liquid, supercooled, and glassy phase (albeit, rapidly quenched) properties over vast compositional spaces with little to no prior knowledge of the underlying systems. In this respect, the identification of GFA indicators and influencing factors relating solely to properties of the amorphous phase is of utmost importance. Moreover, many of the proposed GFA tuning methods and indicators (even those relying only upon single phase properties) exhibit a significant lack of robustness, with their efficacy often either being highly dependent upon the alloy class in question or being limited to specific compositional domains. Fundamentally, these issues can largely be tied to a general neglect of said indicators to consider underlying bonding differences. In this work, a comprehensive comparative analysis of kinetic, thermodynamic, and structural properties in the $Cu_{50}Zr_{50}$ and $Ni_{50}Al_{50}$ alloy systems is conducted using molecular dynamics simulation methods. A key focus of this study is the investigation of underlying connections between the nature of atomic level bonding, short and medium range ordering, and the evolution of structure and transport properties as the two model systems are quenched from the high temperature molten liquid state. While the two alloys under investigation possess similar atomic size ratios and have previously been shown to possess comparable diffusive transport rates in the liquid and supercooled domains, they nonetheless belong to two separate classes of alloys; the transition metal–transition metal (TM–TM) and transition metal–metalloid (TM–M) classes, respectively. As such, the combined analysis of $Cu_{50}Zr_{50}$ and $Ni_{50}Al_{50}$ alloys provides the ideal setting to explore fundamental limitations of the various existing GFA indicators and compositional tuning methods and to potentially facilitate in the identification of new predictive parameters and influencing factors.

II. METHODOLOGY AND COMPUTATIONAL DETAILS

Molecular dynamics simulations were performed using the Large-scale Atomic/Molecular Massively Parallel Simulator (LAMMPS)[19] software package, with atomic interactions described using many-body embedded atom method (EAM) interatomic potentials developed by Mendelev[20] and Mishin[21] for CuZr and NiAl alloys, respectively. Bulk liquid and glassy

phases were generated by first heating randomly ordered systems of 8000 atoms from 300 K to 2300 K over a duration of 1000 ps, followed by a 2000 ps relaxation stage allowing for the proper equilibration of the high temperature liquid melt. Following equilibration, systems were subsequently cooled down to a temperature of 50 K through a series of 25 K quench (100 ps) and hold (150 ps) stages, corresponding to an average linear cooling rate of 0.1 K/ps. Throughout the quenching process, zero pressure isobaric conditions were applied using NPT Nose-Hoover temperature and pressure controls under 1 fs integration time steps. Bulk crystalline phases for both systems were generated and relaxed (similarly under zero pressure barostatic conditions with a 1 fs time-step) at relevant temperatures according to a B2 structured supercell containing 8470 atoms or $35 \times 11 \times 11$ unit cells (following the work of Tang and Harrowell[17]). For both phases in question, property extraction was conducted following further system relaxation at relevant temperatures of interest. Analysis of molecular dynamics simulation results were conducted externally in PYTHON, allowing for the calculation of transport, thermodynamic, and structural properties. More specifically, detailed thermodynamic modeling techniques were used to establish melt/liquidus temperatures and relative phase stabilities throughout the supercooled domain. Using this information, GFA indicators commonly used to quantify the relative phase stability of the amorphous phase such as the reduced glass transition temperature $T_{rg} = T_g/T_l$ and the liquid-crystal free energy difference at glass transition $(\Delta\mu)_{T_g}$ were extracted. Furthermore, volumetric data collected for the crystalline and disordered phases were used to investigate free volume content through the calculation of fractional density differences between the respective phases, $(\rho_c - \rho_{liq})/\rho_c$. Viscous and diffusive transport properties were also sampled along the quenching process, allowing for the assessment of the kinetic fragility parameter $m = (\frac{\partial log_{10}\eta(T)}{\partial(T_g/T)})_{T=T_g}$ and strength parameter D^*, both of which are common GFA indicators serving to differentiate between "strong" and "fragile" glasses based on how abrupt the viscous slowdown is on approach to T_g. Each of these bulk system properties and parameters serves to quantify key influencing factors governing crystallization kinetics in general, namely, the thermodynamic forces driving crystallization and the kinetic factors controlling the rates of crystal nucleation and growth. On the atomic level, short and medium-range chemical and topological ordering was assessed over the quench domain through radical Voronoi tessellation and partial radial distribution function (PRDF) analysis. The evolution of underlying bond anharmonicity and bulk stiffness properties was also investigated in order to assess underlying bonding differences that may elucidate underlying structure-property trends and GFA anomalies. Finally, in an attempt to further connect local bonding differences with observed property trends, short-range cluster statistics were analyzed from a local energy perspective.

A. Thermodynamic and bulk physical property calculations

Thermodynamic properties (entropies and free energies) are obtained using the 2PT method of Lin, Blanco, and Goddard.[22,23] The method allows for the accurate calculation of thermodynamic properties in complex multicomponent systems, requiring short MD simulations of (32 ps used in this study) for the extraction of the atomic vibrational density of states (DOS) through the Fourier transform of atomic velocity autocorrelation functions. System thermodynamic contributions are separated into two components: a harmonically vibrating solid phase and a diffusive hard sphere phase accounting for inherent anharmonicities. The method hinges upon the appropriate decomposition of the vibrational DOS for each component in the mixture into a diffusive gas-like contribution, $S_g(\nu)$, and a harmonically vibrating solid component, $S^s(\nu)$. Once the phase contributions are decomposed, analytic relationships for the thermodynamic properties of the quantum harmonic solid and the diffusive hard-sphere mixture (based on Enskog theory) are utilized for the calculation of total system properties (see Refs. [22] and [23] for a more detailed description of the 2PT methodology).

Melting points (T_m) of the two systems were calculated based on the phase equilibrium condition of equal Gibbs free energy, $\mu_l(T_m) = \mu_c(T_m)$. Following the work of Zhang, An, and Goddard,[24] $\Delta\mu(T_g)$ is utilized in this work as a common metric for evaluating phase stabilities of respective amorphous/supercooled phases, with glass transition temperatures (T_g) estimated by the common intersection point of polynomial fits to low temperature and high temperature enthalpy data (see the works of Zhang *et al.*[24] and Mendelev *et al.*[20]).

Second order thermodynamic properties (constant volume/pressure heat capacities and thermal expansion coefficient) were calculated through two different methods: direct calculation of enthalpy/energy and volume temperature derivatives through symmetric finite differencing of cooling curve data, and second, through the fluctuations approach as expressed in the following relations:

$$C_p \equiv \left(\frac{\partial H}{\partial T}\right)_P = \frac{1}{k_B T^2}\langle\delta H^2\rangle_{NPT},$$

$$C_v \equiv \left(\frac{\partial U}{\partial T}\right)_V = \frac{1}{k_B T^2}\langle\delta U^2\rangle_{NVT},$$

$$\alpha_T \equiv \left(\frac{\partial V}{\partial T}\right)_P = \frac{1}{k_B T^2}\langle\delta V^2\rangle_{NPT}.$$

Similarly, the fluctuations approach was utilized for the calculation of isothermal compressibility, β_T (or inverse bulk moduli, B_T),

$$\beta_T = B_T^{-1} \equiv -\frac{1}{V}\left(\frac{\partial V}{\partial T}\right)_T = \frac{1}{k_B T}\frac{\langle\delta V^2\rangle_{NPT}}{\langle V\rangle_{NPT}}.$$

Utilizing these results, (pseudo)Gruneisen parameters were subsequently calculated through the following relation:

$$\gamma = \frac{\alpha_T B}{C_v \rho}.$$

While the two calculation methods yielded consistent results, values obtained through the fluctuation method were found to exhibit more noise. Subsequently, for the calculation of (pseudo)Gruneisen parameters, heat capacities and thermal expansion coefficients corresponding to those directly obtained from cooling curve data were used.

B. Transport property and fragility calculations

Equilibrium Green-Kubo methods are used for the calculation of atomic diffusivities and shear viscosities in both systems under study. Under the Green-Kubo formalism, atomic diffusivities are directly related to the velocity autocorrelation function through the following relation:

$$D = \frac{1}{3} \int_0^\infty \langle v(t+t') \cdot v(t) \rangle dt'.$$

Denoting the velocity power spectral density as $P(\nu)$, the diffusion coefficient can be equivalently expressed in terms of the zero frequency power spectral density,

$$P(0) = \int_{-\infty}^\infty \langle v(t+t') \cdot v(t) \rangle e^{-2i\pi(0)} dt'$$

$$= 2 \int_0^\infty \langle v(t+t') \cdot v(t) \rangle dt' = 2D$$

$$\Rightarrow D = P(0)/2.$$

An initial 300 ps relaxation run, followed by a 32 ps velocity sampling run under NVT conditions, was found to be sufficient for proper convergence of diffusivities.

Similarly, viscosities are directly related to the stress autocorrelation functions $\langle P_{\alpha\beta}(t)P_{\alpha\beta}(0) \rangle$ through the following relation:

$$\eta = \frac{V}{kT} \int_0^\infty \sum_{\alpha\beta} \langle P_{\alpha\beta}(t)P_{\alpha\beta}(0) \rangle dt,$$

where $P_{\alpha\beta}$ is the symmetrized traceless portion of the stress tensor $\sigma_{\alpha\beta}$, defined as[25]

$$\sigma_{\alpha\beta} = \frac{1}{V} \sum \left[\frac{p_{i,\alpha}p_{i,\beta}}{m_i} + (r_{i,\alpha})(F_{i,\beta}) \right],$$

$$P_{\alpha\beta} = \frac{1}{2}(\sigma_{\alpha\beta} + \sigma_{\beta\alpha}) - \frac{1}{3}\delta_{\alpha\beta}\left(\sum_y \sigma_{yy}\right).$$

The above formulation averages over the five independent components of the traceless stress tensor P_{xy}, P_{yz}, P_{zx}, $\frac{1}{2}(P_{xx} - P_{yy})$, and $\frac{1}{2}(P_{yy} - P_{zz})$ (with the last two being equivalently to the first three by rotational invariance[26]), allowing for improved autocorrelation function statistics. In order to acquire sufficient convergence of stress autocorrelation functions, simulation runs ranged from 1000-3000 ps (under 1 fs time steps), ensuring sampling times of at least 50 times underlying relaxation times.

Kinetic fragility (m) and strength parameter (D^*) are extracted through viscosity fitting to the Vogel-Fulcher-Tammann (VFT) form,

$$\eta(T) = \eta_0 exp\left(\frac{D^*T_0}{(T-T_0)}\right),$$

where η_0 is the high temperature viscosity limit, T_0 is the divergent temperature (often close in value to Kauzmann temperature T_K), and D^* is the strength parameter, a common fragility metric with larger D^* indicative of stronger glasses. The above VFT form was fit to viscosity data collected in 25 K intervals over a temperature range of 1.2–1.8T_g. Once the VFT fit parameters are extracted, the kinetic fragility parameter m is

also determined through the following relation:

$$m = \left(\frac{\partial log_{10}\eta(T)}{\partial(T_g/T)}\right)_{T=T_g} = \frac{T_g * D^*T_0}{log(10)} \frac{1}{(T_g - T_0)^2}.$$

However, due to the significantly higher cooling rates experienced under the simulated quench, the standard rheological definition for the glass transition temperature based on viscosities equalling 10^{12} Pa s is neither appropriate for arriving at consistency with the calorimetric T_g extracted from the thermodynamic cooling curve results nor for obtaining representative estimates of liquid fragilities using the above relation (for which fragilities will be artificially over-valued). In order to partially account for associated cooling rate effects, a rescaling of the rheological condition for the glass transition temperature from $\eta(T_g) = 10^{12}$ Pa s to $\eta(T_g) = 10^3$ Pa s is implemented in the present study.

The physical basis for this rescaling can be understood by first considering that the process of glass formation is intrinsically linked to the competition between underlying internal (structural, enthalpic, etc.) relaxation times (τ_{int}) governing equilibrium kinetics and experimental/observational time scales (τ_{obs}) acting to limit the extent of relaxation and configurational sampling possible. With experimental time scales being inversely proportional to the cooling rate ($\beta = \frac{dT}{dt}$) at any given temperature and pressure along the quench, system dynamics are seen to effectively be frozen out below some temperature T_g, where $\tau_{int}(T_g) \approx \tau_{obs}$. Considering that viscosities governing bulk shear/structural relaxation are proportionally dependent upon underlying shear relaxation times ($\eta \propto \tau_{shear}$), this condition is generally satisfied for the majority of liquid melts under standard experimental operating conditions (where $\tau_{obs} \approx 10^2$–10^3 s) when viscosities are on the order of 10^{12} Pa s, hence the standard rheological condition for the glass transition temperature: $\eta(T_g) = 10^{12}$ Pa s. Based on these fundamental principles underlying the glass transition phenomena in general, we arrive at the following scaling law for viscosities at T_g under simulated cooling rates:

$$\eta(T_g) \propto \tau_{shear}(T_g) \approx \tau_{obs} \propto \frac{1}{\beta}$$

$$\rightarrow \frac{\eta(T_g)|_{\beta_{sim}}}{\eta(T_g)|_{\beta_{exp}}} = \frac{\tau_{sim}}{\tau_{exp}} = \frac{\beta_{exp}}{\beta_{sim}}.$$

With $\eta(T_g)|_{\beta_{exp}} = 10^{12}$ Pa s corresponding to standard experimental operating conditions where cooling rates are on the order of $\beta_{exp} \approx 10^2$ K/s and with simulated cooling rates utilized in this study being $\beta_{sim} = 10^{11}$ K/s, we arrive at the stated rescaled viscosity condition

$$\eta(T_g)|_{\beta_{sim}} = (10^{12} \text{ Pa s}) * \frac{(10^2 \text{ K/s})}{(10^{11} \text{ K/s})} = 10^3 \text{ Pa s}.$$

In order to differentiate between the calorimetric T_g estimated from cooling curve data in the remainder of this paper, the rheological glass transition temperature defined by this rescaled viscosity condition will be denoted by $T_g^{\eta=10^3 \text{ Pa s}}$.

C. Structural property calculations

Partial radial distribution functions ($g_{\alpha\beta}$) are calculated through standard binning techniques formally expressed in the

following relation:

$$g_{\alpha\beta}(r) = \frac{V}{N_\alpha N_\beta} \langle \sum_{i=1}^{N_\alpha} \frac{n_{i\beta}(r)}{4\pi r^2 \Delta r} \rangle.$$

0.1 A bin sizes were used ($\Delta r = 0.1$ A), and in order to improve statistics, PRDF results were averaged over 5 separate snapshots (taken over a 32 ps duration).

Short-range ordering and structure is primarily investigated through the analysis of radical Voronoi tessellation results. Voronoi tessellation involves the decomposition of the system into a finite number of polyhedra centered about the various atomic sites, with volumes encompassed by each polyhedra consisting of the set of all points closer to that given atomic center than any other. In standard Voronoi tessellation, polyhedra edges correspond to the intersection of planes positioned at the perpendicular bisector connecting neighboring atomic centers, with faces corresponding to the common area shared by both atoms. Radical Voronoi tessellation generalizes the above framework to polydisperse systems by scaling plane positions according to the ratios of atomic radii. Polyhedra types are subsequently differentiated according to their Voronoi indices $\langle n_3, n_4, n_5, n_6, \ldots, n_1 0 \rangle$, where n_i denotes the number of i-edged faces possessed by the given Voronoi polyhedron (with i ranging from 3 to 10 due to geometrical constraints). As each face corresponds to a "bond" between the central and corresponding atomic neighbor, coordination number (CN) can be determined by summing the total number of faces, or $CN = \sum_i n_i$. In this study, radical Voronoi tessellation is conducted through the Voro++ package.[27] System snapshots are taken every 512 time steps over a sampling duration of 32 ps allowing for improved cluster statistics.

Atomic nearest-neighbour information extracted from Voronoi tessellation were further utilized for the investigation of local compositional ordering through calculation of the Warren-Cowley parameter. Denoting $\langle CN \rangle$ as the mean total coordination number (or mean number of nearest-nearest neighbours), $\langle CN_{ij} \rangle$ the mean coordination of species j atoms about species i central atoms, and c_i the bulk stoichiometric concentration of species i, the Warren-Cowley parameter α_p is calculated through the following relation:

$$\alpha_p = \frac{c_i \langle CN \rangle - \langle CN_{ji} \rangle}{c_i \langle CN \rangle} = \frac{c_j \langle CN \rangle - \langle CN_{ij} \rangle}{c_j \langle CN \rangle}$$

viewing the relation above, the Warren-Cowley parameter serves to quantify the average deviation of local compositions (comprised of atoms in the first coordination shell) from that of the bulk (stoichiometric composition). Greater local compositional deviations from bulk stoichiometry is a signature of enhanced compositional short-range ordering (CSRO) in the amorphous phase.[28]

III. RESULTS AND DISCUSSION

Molecular dynamics simulations of amorphous and B2 crystalline phases for both NiAl and CuZr systems were conducted and sampled along the various temperatures of interest. Liquid and glassy phases were generated through rapid quenching of initial equilibrated melts at temperatures of 2100 K and 2300 K, respectively, for CuZr and NiAl (roughly encompassing a temperature domain up to $3T_g$ for both systems). Thermodynamic, physical, transport, and structural properties were subsequently sampled (following 300 ps relaxation runs) in 25 K intervals as the system was quenched down to 50 K, with results presented below in Secs. III A–III D.

A. Bulk thermodynamic and physical properties

Gibbs free energy curves for the amorphous and crystalline phases are presented in Figure 1. Based on the point of intersection of liquid and crystal phase free energy curves, melting points are calculated to be 1557 K and 1355 K for the NiAl and CuZr systems, respectively. For quick validation of the 2PT modeling, these values are seen to be in close agreement with the estimates of Tang and Harrowell[17] of 1535 K and 1340 K obtained through the condition of equilibrated coexistence for liquid and crystal phases in planar contact. Moreover, glass transition temperatures (T_g) of 740 K and 676 K for
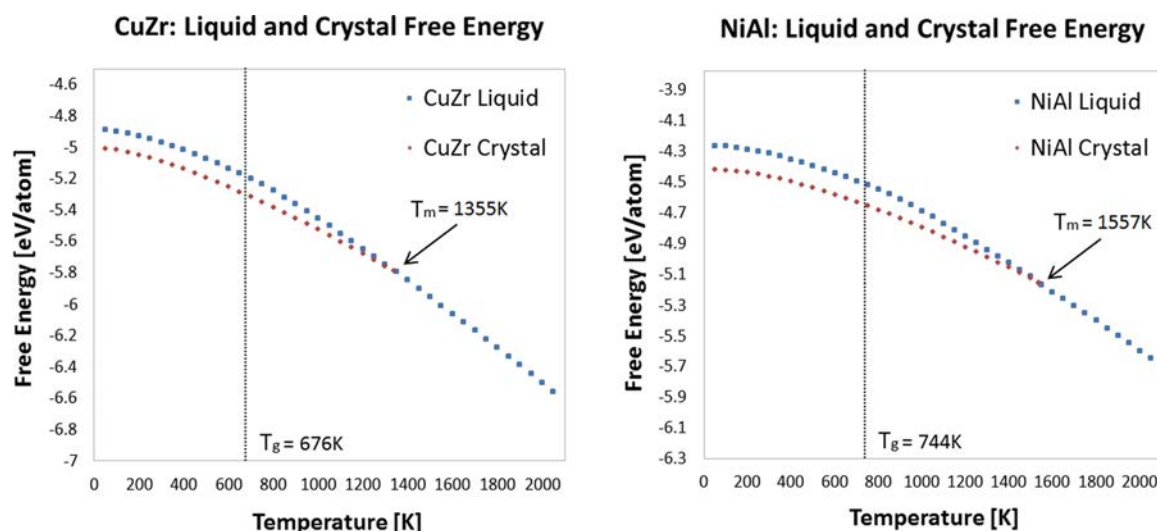

FIG. 1. Gibbs free energy profiles for liquid/amorphous and B2 crystalline phases CuZr (left) and NiAl (right) calculated from 2PT modeling. Vertical dashed lines correspond to respective T_g values. Melting points (T_m) are identified by the intersection of liquid/amorphous and crystalline phases.

TABLE I. Summary of thermodynamic and bulk physical property results.

	T_g (K)	T_m (K)	T_{rg}	Δh_m (eV/atom)	Δs_m (eV/K−atom)	$\Delta \mu(T_g)$ (eV/atom)
NiAl	744	1557	0.48	0.233	0.000 150	−0.135
CuZr	676	1355	0.50	0.200	0.000 148	−0.116

NiAl and CuZr systems were extracted using enthalpy cooling curve data (see computational details). While experimental T_g values for the NiAl system are unavailable due its rapid crystallization rate, CuZr's computed T_g value is seen to be in direct agreement with Russew's[16] experimentally determined T_g value of 676 K based on viscosity data. Utilizing these results, reduced glass transition temperatures ($T_{rg} = T_g/T_m$) and liquid-crystal free energy differences at T_g ($\Delta\mu(T_g)$) are evaluated, yielding values of 0.48 and −0.116 eV/atom for CuZr and 0.50 and −0.135 eV/atom for NiAl. Comparison of these results (summarized in Table I) yields quantitative evidence for the lower thermodynamic phase stability of the NiAl amorphous phase.

Moreover, presented in Figures 2 and 6, constant pressure heat capacities ($C_P = (\frac{\partial H}{\partial T})_P$) as well as thermal expansion coefficients ($\alpha_T = \frac{1}{V}(\frac{dV}{dT})_P$) for NiAl and CuZr amorphous phases are plotted. Viewing the results, it can be seen that NiAl system undergoes a more dramatic C_P drop on approach to T_g, indicating the freezing out of a higher density of states in the deeply supercooled domain.[29] Based on the energy landscape considerations of Angell, Ito, and Moynihan,[30,31] the NiAl system would therefore be associated with a higher thermodynamic fragility than CuZr, results consistent with existing correlations between thermodynamic/kinetic fragility and GFA.

B. Transport and kinetic properties

Results of calculated atomic diffusivities and shear viscosities are presented in Figure 3. In order to quantitatively assess kinetic fragilities, viscosity data were fit to the VFT form,

$$\eta(T) = \eta_0 exp(\frac{D^* T_0}{(T - T_0)}),$$

where η_0 is the high temperature viscosity limit, T_0 is the divergence temperature (often close in value to the Kauzmann
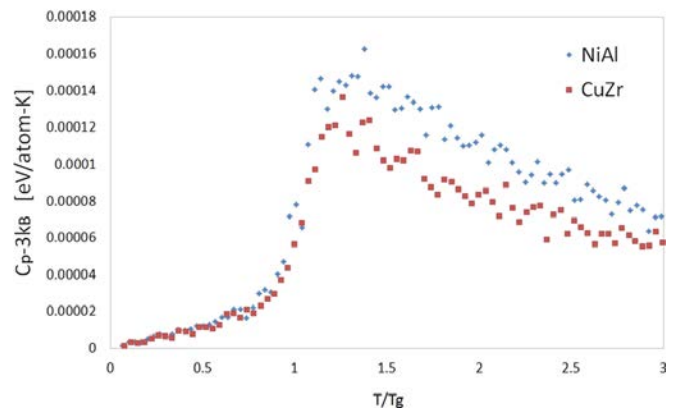

FIG. 2. Constant pressure heat capacity (C_P) of NiAl and CuZr amorphous phases. Harmonic approximations are used to partially account for low temperature C_P quantum contributions through the subtraction of $3k_B$.

temperature T_K), and D^* is the strength parameter. Kinetic fragility parameters ($m = (\frac{\partial log_{10}\eta(T)}{\partial(T_g/T)})_{T=T_g^{\eta=10^3\ Pa\ s}}$) were further estimated by interpolating viscosities down to a rheological glass transition temperature $T_g^{\eta=10^3\ Pa\ s}$ identified by the rheological condition that $\eta(T_g) = 10^3$ Pa s (see Section II B for a detailed discussion of the physical basis for using this alternative viscosity condition instead of the standard rheological condition of $\eta(T_g) = 10^{12}$ Pa s which applies under experimental conditions). These results, in conjunction with estimated rheological glass transition temperatures ($T_g^{\eta=10^3\ Pa\ s}$), are summarized in Table II.

Comparing strength and kinetic fragility parameters (D^* = 2.07 and 1.58, m = 61.4 and 75.5, respectively, for NiAl and CuZr), both values indicate the NiAl system to be the kinetically stronger system, an unexpected result considering NiAl's lower GFA and thermodynamic fragility. Interestingly, as is illustrated by CuZr's significantly higher η_0 value of 15.2×10^{-4} Pa s in comparison to NiAl's 9.8×10^{-4} Pa s, NiAl's lower fragility is largely non-reflective of traditional correlations to high temperature melt atomic mobilities. Investigation into high temperature property variations reveals that near respective melting points, NiAl diffusivities are about 1.6-1.7 times that of CuZr and CuZr viscosities are approximately 1.2-1.3 times higher than NiAl. Quite surprisingly however,
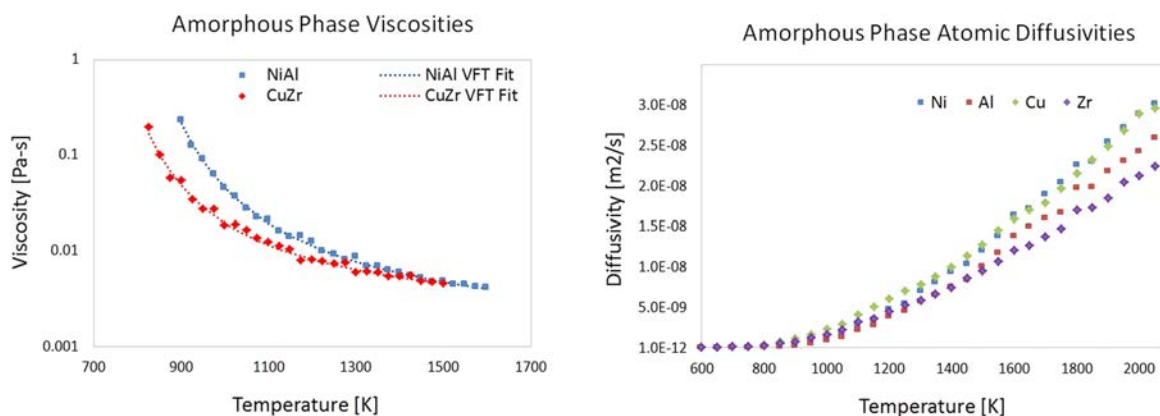

FIG. 3. Viscosity and atomic self-diffusivities for $Ni_{50}Al_{50}$ and $Cu_{50}Zr_{50}$ alloys over the quench regime.

TABLE II. Viscosity VFT fit and fragility results.

	η_0 (10^{-4} Pa s)	T_0 (K)	$T_g^{\eta=10^3 \text{ Pa s}}$ (K)	D^*	m
NiAl	9.77	650	748	2.07	61.4
CuZr	15.22	617	690	1.58	75.5

FIG. 4. Atomic diffusivities scaled by respective atomic radii squared in $Ni_{50}Al_{50}$ and $Cu_{50}Zr_{50}$ alloys over the quench regime.

while CuZr appears to possess lower atomic mobilities in the high temperature melt, a dramatic drop in NiAl transport rates is observed upon entering the supercooled domain, resulting in lower atomic mobilities for NiAl throughout much of the supercooled temperature region, and subsequently, a lower kinetic fragility. Further compounding these discrepancies, accounting for the approximately 10 percent shorter (average) atomic jump distances expected in the NiAl system (due to the smaller atomic radii of Ni and Al in comparison to Cu and Zr), transport rates for the NiAl system are effectively under-represented. This can more clearly be seen by scaling atomic diffusivities by associated squared atomic radial distances, with results of such scaling illustrated in Figure 4 (with temperatures also scaled by respective T_g values). While also apparent in the unscaled diffusivity plots, scaled Zr atomic diffusivities are seen to be significantly lower than Cu atoms, indicative of enhanced decoupling between diffusive and viscous transport in the CuZr amorphous phase (Stoke-Einstein breakdown) and likely reflective of more collective flow behavior.

Investigating thermal stabilities through a kinetic perspective, fractional density differences $((\rho_c - \rho_{liq})/\rho_c)$ between respective amorphous and crystalline phases are calculated over relevant temperatures of interest and plotted in Figure 5. Based on free volume theory, one would expect the higher atomic mobilities observed for NiAl in the high temperature melt regime to correspond with poorer atomic packing efficiencies and higher free volume content. These notions are consistent with the fractional density differences calculated with results revealing the presence of anomalously large volume differences between the NiAl amorphous and crystalline phase. Summarized in Table III, fractional liquid-crystal density differences observed for the NiAl system range from 7%–11% along the quench, corresponding to values 2-3 times that of the CuZr system. The 10% volume change observed at
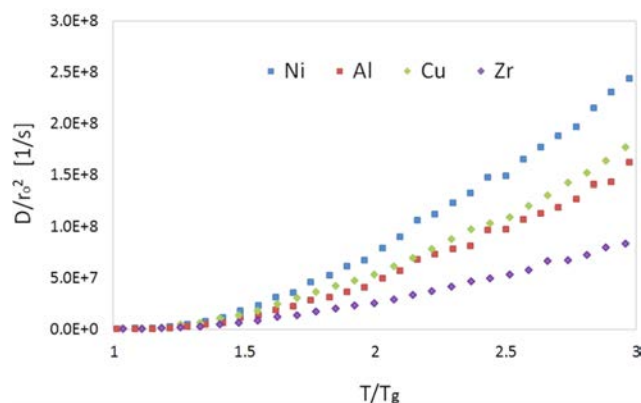
T_m in the NiAl system marks a significant departure from the 0%–3% volume change characteristic of good glass forming systems.[32,33] With that said, these results are suggestive of primarily kinetic origins to NiAl's poor GFA, likely associated with underlying bond frustration and packing inefficiencies in the amorphous phase.

The lower kinetic fragility of the NiAl system is a highly surprising result considering the previous thermodynamic fragility analysis as well as existing fragility-GFA correlations. However, considering the remarkably large fractional volume differences observed between NiAl amorphous and crystal phases, along with the significant volume contraction experienced over the quench domain, it is possible that observed transport property trends in the NiAl system may be explained by consideration of the inter-atomic interaction changes and associated bond-strain effects. In order to explore this concept, bulk moduli ($B = -V(\frac{dP}{dV})_T$), constant volume heat capacities ($C_v = (\frac{dU}{dT})_V$), and thermal expansion coefficients ($\alpha_T = \frac{1}{V}(\frac{dV}{dT})_P$) were independently calculated, allowing for the calculation of amorphous phase Gruneisen parameters (γ) through the following thermodynamic relation:

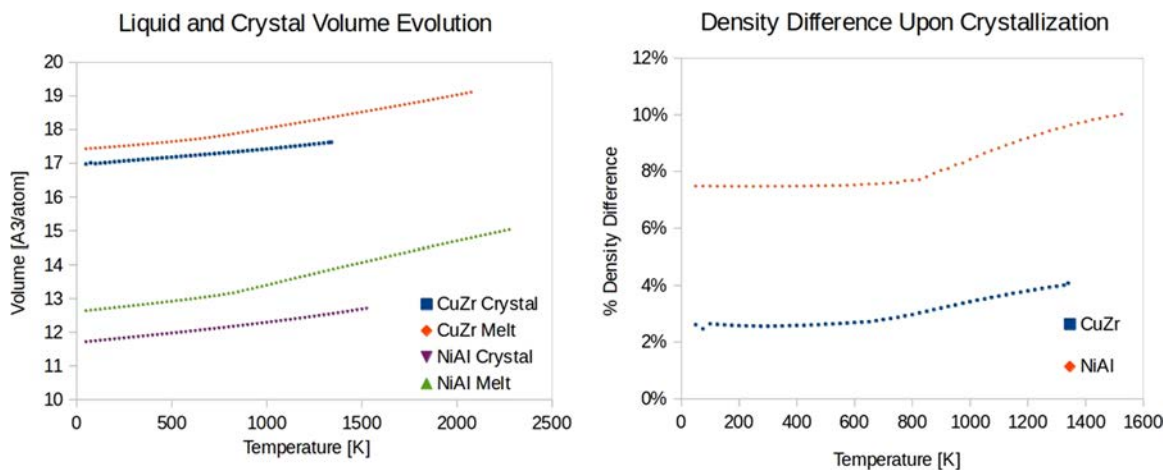$$\gamma = \frac{\alpha_T B}{C_v \rho}.$$

FIG. 5. Percent density difference between the liquid/glassy and B2 crystalline phases for NiAl and CuZr alloys over the quench regime.

TABLE III. Fractional liquid-crystal density differences at T_g and T_m.

	$\frac{\Delta\rho_{lc}}{\rho_c}(T_g)$	$\frac{\Delta\rho_{lc}}{\rho_c}(T_m)$
NiAl (%)	7.60	10.04
CuZr (%)	2.75	4.08

Fundamentally, the Gruneisen parameter quantifies underlying bonding stiffness (or vibrational frequency) dependencies on volume/strain and is defined as

$$\gamma = -\frac{V}{\omega}\frac{d\omega}{dV} = -\frac{r}{6k}\frac{dk}{dr},$$

where ω is the phonon frequency, k is the interatomic force constant (bond stiffness), V is the volume, and r is the interatomic separation. As noted by Fultz,[34] assuming a Gruneisen parameter $\gamma \approx 2$, the above relations would subsequently predict an inter-atomic force change of -12% given an interatomic distance change of only 1%. As such, the Gruneisen parameter is highly relevant to the analysis of bonding in the amorphous phase where inter-atomic separation distances are variable from atom to atom.

First, focusing on resultant property variations in the liquid and supercooled domains (see Figure 6), CuZr Gruneisen parameters are found to undergo a near monotonic decay from the high temperature value of $\gamma \approx 1.65$ down to a value of $\gamma \approx 1.35$ at the glass transition temperature. A monotonically decreasing profile would be expected in the case that underlying structural and chemical reordering taking place along the quench is conducive to the improvement of atomic level bonding and packing configurations (thereby leading to reduced bond strain and anharmonicity). In contrast, the NiAl system experiences the opposite Gruneisen parameter trends. NiAl Gruneisen parameters are seen to increase from $\gamma \approx 2.0$ up to

a maximum of approximately 2.5-3.0 just above T_g, followed by a sudden drop to a value of ≈ 2.05 at T_g. These differences continue down into the low temperature glassy domains where the monotonically decreasing Gruneisen profile observed in the CuZr melt domain is observed to continue down to minimum of $\gamma \approx 0.9$, while NiAl Gruneisen parameters more or less persist at a constant value of $\gamma \approx 2.0$. Interestingly, clear differences are also observed upon comparison of respective bulk moduli profiles. Nearly identical NiAl and CuZr bulk moduli are observed down to temperatures of about $1.3T_g$, upon which a sudden departure is observed among the two systems. Near $T \approx 1.3T_g$, a sudden bulk moduli increase persisting down to T_g is observed in the NiAl system, indicative of substantial changes in underlying stiffness and bonding properties. Moreover, it is apparent that $1.3T_g$ also corresponds to peak thermal expansion coefficients and thus to the region of greatest volumetric temperature sensitivity and contraction. Combined, these results suggest a strong connection between relaxation properties and underlying mechanical ordering associated with bond anharmonicity and strain-volume dependencies in the NiAl system. In accordance with the large Gruneisen parameters observed in the NiAl system, the large volume contraction observed over the supercooled domain would have the side effect of substantial bond stiffness increases, ultimately reflected through higher structural relaxation times near T_g and a correspondingly lower fragility. In the high temperature melt, the NiAl system likely experiences significant local bond strain and mismatch as evidenced by fractional liquid-crystal volume differences in excess of 10%, in contrast to volume differences 2-3 times lower in the CuZr system.

Considering CuZr and NiAl systems belong to two separate classes of alloys, the question arises as to whether the observed anharmonicity and bonding differences can be generalized to be attributes of TM–TM and TM–M bonding as
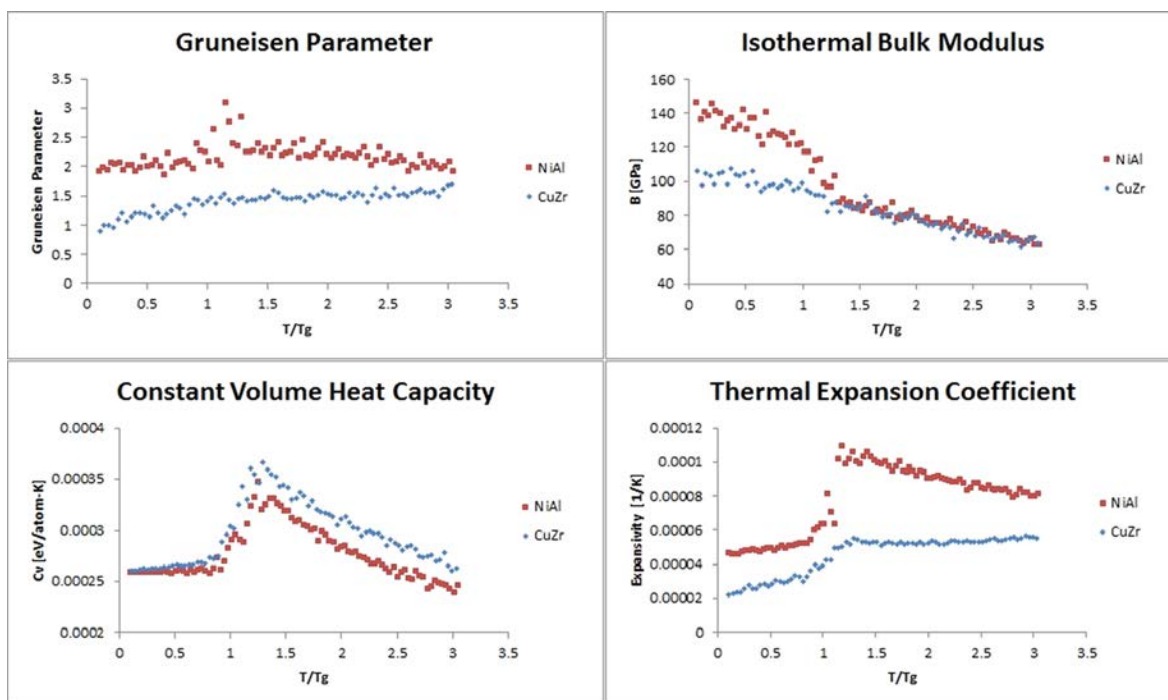

FIG. 6. Second order thermodynamic properties and resultant Gruneisen parameters for $Ni_{50}Al_{50}$ and $Cu_{50}Zr_{50}$ amorphous phases over the quench regime.
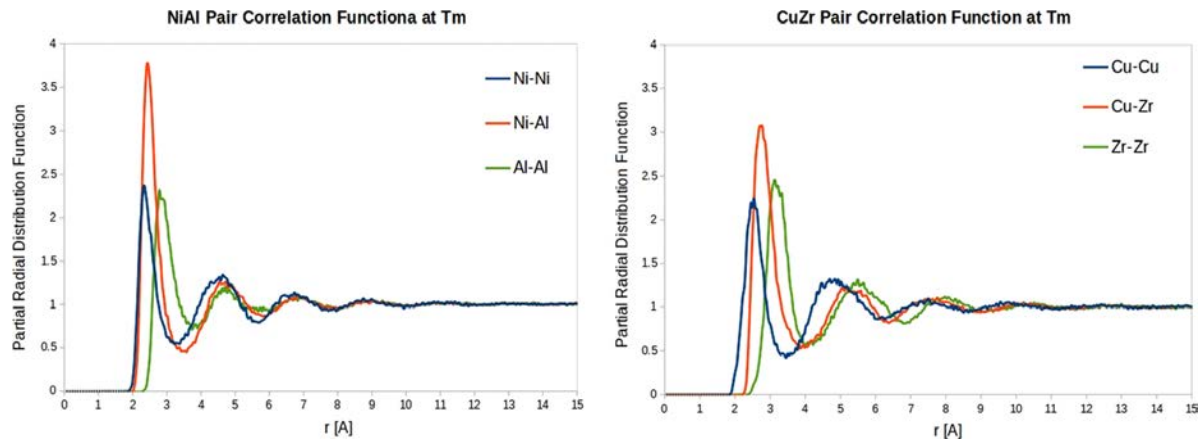
FIG. 7. Pair correlation functions evaluated for $Ni_{50}Al_{50}$ and $Cu_{50}Zr_{50}$ melts at temperature $T \approx 2 * T_g \approx T_m$.

a whole, or whether they are specific to the given alloys in question. Moreover, a reasonable expectation would be for the observed differences in bonding, transport, and kinetic properties to be reflected in the nature and evolution of short and medium range structure over the quench. With this in mind, an in-depth investigation of short/medium-range chemical and topological ordering is conducted in Sec. III C, largely aimed at the search for key structural signatures of underlying bonding differences.

C. Structural analysis

In order to assess medium-range ordering differences, pair correlation functions were computed for both systems, with results evaluated near respective melt temperatures (1400 K and 1600 K for CuZr and NiAl, respectively) presented in Figure 7. Analyzing the figures, density correlations extending from the nearest-neighbor to next-nearest-neighbor coordination shells are seen to much more rapidly decay in the NiAl system, most notably apparent upon comparison of the ratio of first and second peak heights (summarized in Table IV) for Ni–Al and Cu–Zr pair-correlation functions (3.05 and 2.50, respectively). In conjunction with these observations, the high first peak intensities and large extent of bond-length shortening observed suggest significantly more pronounced Ni–Al nearest-neighbor level interactions. Looking beyond the first peak, relatively weak Ni–Ni, Ni–Al, and Al–Al density correlations with nearly identical profiles are observed, indicating a low degree of medium-range compositional ordering. In contrast, longer-ranged next-nearest-neighbor interactions appear much more pronounced in the CuZr system, with strong and largely non-overlapping density correlations extending well into the 2nd, 3rd, and even 4th coordination shells.

TABLE IV. Ratio of first and second partial radial distribution peak intensities.

	$g_{AA}(r_1)/g_{AA}(r_2)$	$g_{AB}(r_1)/g_{AB}(r_2)$	$g_{BB}(r_1)/g_{BB}(r_2)$
NiAl	1.78	3.05	1.92
CuZr	1.70	2.50	1.92

Notably, these observations are consistent with metal-metal (TM–TM) and metal-metalloid (TM–M) bonding in general. Belonging to the TM–TM alloy class (and associated with copper's noble metal electronic state), Cu–Zr bonding would be expected to be longer-ranged and less directional. In contrast, TM–M bonding is characteristically more covalent/short-ranged and directional, consistent with the observed Ni–Al bond-length shortening, pronounced nearest-neighbor level interactions, and weak next-nearest-neighbor interactions. Thus, a simple phenomenological explanation for the observed Gruneisen and bulk moduli anomalies in the NiAl system can be formulated based on these expected bonding differences. Mismatch between underlying strain-stiffness dependencies of Ni–Al, Ni–Ni, and Al–Al partial bonds inhibits bulk structural relaxation to globally efficient packing structures in the high temperature Ni–Al melt. Subsequently, the high temperature NiAl melt exhibits high free volume content and high diffusive and viscous transport rates. As the system is cooled, associated volume contraction results in significantly increased interactions among previously "non-bonded" or poorly bonded Ni–Al atoms, translating to a sudden spike in bulk stiffness properties (bulk moduli), viscosities, and ultimately to a lower kinetic fragility. On the other hand, bonding in the CuZr system is longer-ranged, less directional, and highly metallic in character, translating to minimal short-range bonding constraints, and promoting global structural relaxation (through more cooperative flow rearrangements) to lower free volume packing configurations. In this respect, while the NiAl system exhibits a lower kinetic fragility than CuZr, it is largely an artifact of underlying volume-strain and bond-stiffness dependencies. Interestingly, as previously noted by Suryanarayana and Inoue,[35] the efficacy of the fragility parameter as a direct measure of GFA is highly dependent upon the respective alloy class in question. Namely, while the fragility (strength) parameter D^* has been identified to act as a direct measure of GFA in BMGs with purely metallic components,[36,37] it largely breaks down as a reliable GFA indicator in systems containing metalloid species.[38]

Results of radical Voronoi tessellation analysis of short-range topological and compositional ordering in the two systems were similarly found to be reflective of such underlying
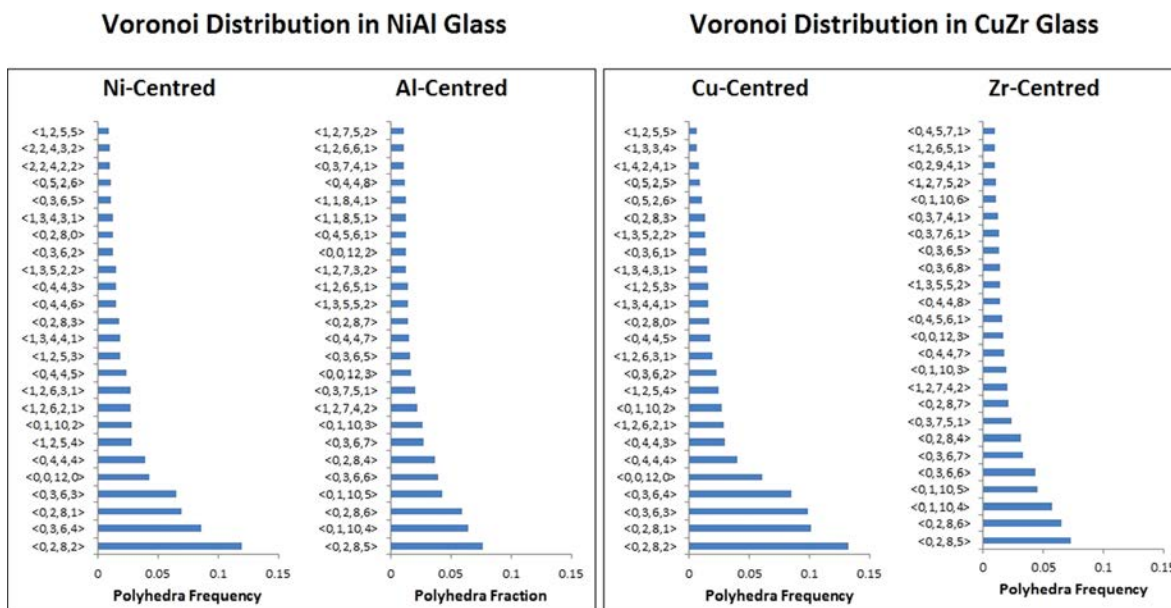
FIG. 8. Top 25 most frequent Voronoi polyhedra types in NiAl and CuZr glasses at 300 K.

bonding differences. Starting with nearest-neighbor cluster/polyhedra and coordination number distributions (Figures 6 and 8) in respective NiAl and CuZr glasses at 300 K, results are presented in Figures 8 and 9. At first glance, cluster and coordination distributions in respective glassy phases appear strikingly similar. However, further inspection reveals a number of revealing differences reflective of the short-range versus long-range bonding properties of NiAl and CuZr systems. Higher icosahedral ordering is observed in the CuZr system (a signature of longer-ranged interactions and enhanced thermal stability of the amorphous phase), with higher fractions of $\langle 0,0,12,0 \rangle$, $\langle 0,2,8,2 \rangle$, and $\langle 0,2,8,1 \rangle$ clusters. The coordination distributions in the CuZr system are also seen to be more

tightly distributed among CN = 12 for Cu and CN = 16 for Zr atoms, with less respective coordination overlap and CN = 14 clusters overall in comparison to the NiAl system. Considering the B2 crystal phase is entirely composed of CN = 14 short-range clusters, these observations are suggestive of enhanced compositional ordering in the CuZr system, with greater short-range structural overlap between the amorphous and crystal phases in the NiAl system.

Further investigating CSRO, the evolution of the Warren-Cowley parameter[28] has been evaluated in both systems over the quench domain, with results presented in Figure 10. The Warren-Cowley parameter serves as a common metric for CSRO, with large (negative) values being indicative of
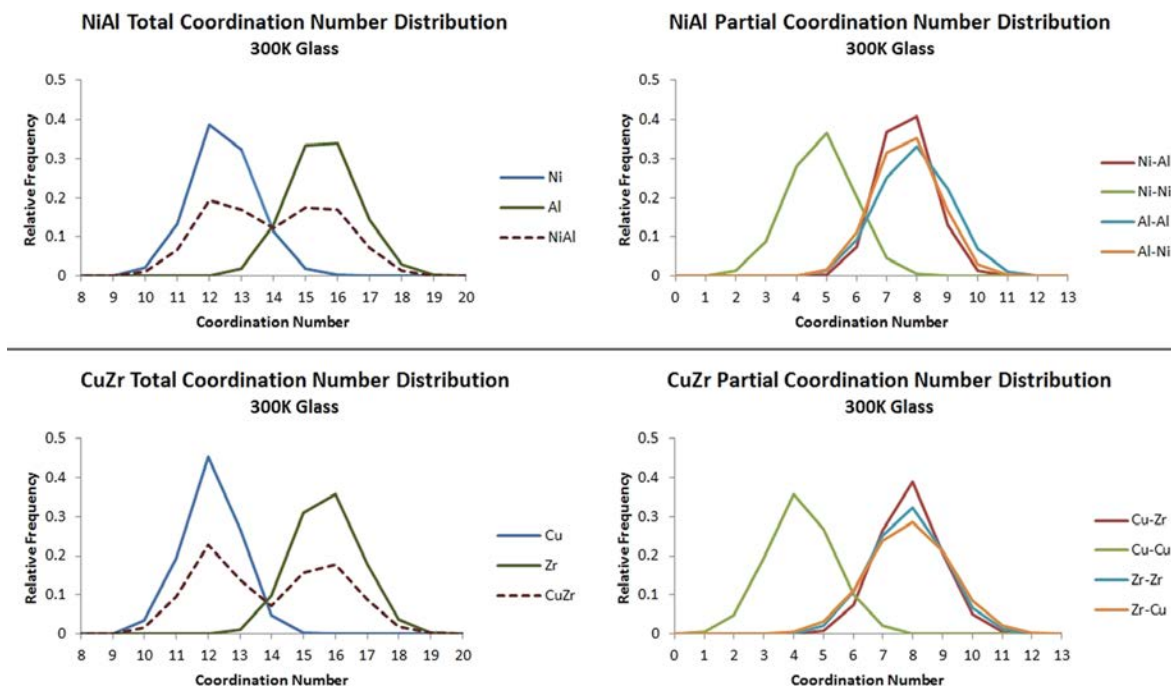

FIG. 9. Partial and total coordination number distribution for atoms in NiAl and CuZr glasses at 300 K.
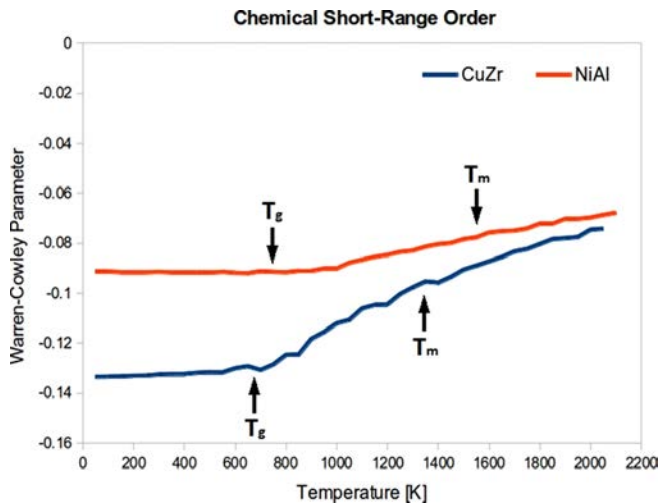
FIG. 10. Evolution of local compositional ordering over the quench for CuZr and NiAl alloys. The Warren-Cowley parameter is a simple metric quantifying the deviation of the local composition (first coordination shell) from the bulk stoichiometric concentration.

FIG. 11. Mishin's EAM embedding energy functions for Ni and Al atoms[21] in the equilibrium B2-NiAl phase.

significant deviations of local compositions from bulk stoichiometry (see Sec. II C as well as Ref. 28 for further details on the Warren-Cowley parameter). Significantly enhanced CSRO is apparent in the CuZr system. Interestingly, while associated chemical reordering taking place in the CuZr system is seen to freeze out at T_g as expected, the corresponding freeze-out temperature in the NiAl system is seen to occur near 950-1000 K or $\approx 1.3T_g$. Referring to Figure 6, it is apparent that the observed NiAl CSRO freeze-out temperature coincides instead with the bulk moduli departure temperature (as well as the temperature domain associated with peak expansivity). Subsequently, the strong bond strain-stiffness dependencies previously identified in the NiAl system are seen to have the negative side-effect of inhibiting compositional short-range ordering in the amorphous phase, a likely contributing factor to NiAl's lower GFA.

D. Local structure-energy correlations

Interestingly, viewing Mishin's EAM embedding functions (reproduced[21] in Figure 11) for Ni and Al atoms, the Ni embedding function is seen to exhibit a minimum near mean electron densities in accordance with the traditional convex parabolic shaped profile characteristic of metallic elements. In contrast, at mean electron densities, the Al embedding energy function is seen to exhibit a maximum with an apparent minimum present in the low density regime and a sharp decreasing profile observed in the higher density regime. These observations further elucidate underlying bonding differences and are suggestive of highly variable bonding/stiffness properties of Al depending on bond strain and local coordination/compositions. The Al embedding function minimum present in the lower density regime is likely to be the source of the poor amorphous phase packing efficiencies observed in the NiAl system, with the bulk moduli spike observed being associated with volume/strain contraction linked to the sharp decreasing energy profile in the higher local electron density domain. Considering the previous analysis of structural, kinetic, and
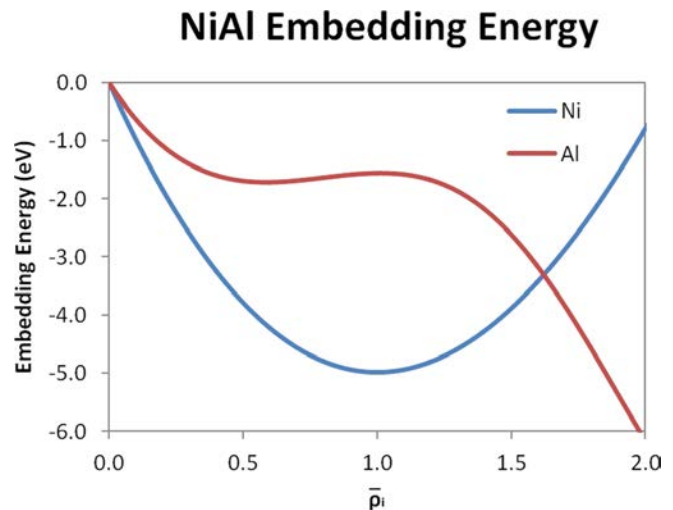
bonding property differences in the two systems, Ni–Al bond-length shortening and mismatch between underlying strain-stiffness dependencies of Ni–Al, Ni–Ni, and Al–Al partial bonds introduce significant local bonding constraints which act to inhibit bulk structural relaxation and the attainment of globally efficient packing structures in the amorphous phase. The more metallic (non-directional, longer-ranged) bonding properties of the CuZr system on the other hand promote more collective relaxation behavior, driving topological and chemical reordering towards locally and globally efficient packing configurations. An interesting question is whether such bonding differences are discernible through the analysis of local per-atom potential energies. Probing the degree at which local energetics influence short-range structural ordering in the two systems, statistics on the local atomic potential energies of atoms were collected and analyzed at various temperatures of interest along the quench. Subsequently, mean (local atomic) potential energies for central atoms belonging to the various Voronoi polyhedra types sampled were evaluated and correlations with Voronoi polyhedra occupation probabilities (cluster distributions) were assessed. Results of this analysis for Ni, Al, Cu, and Zr centered clusters at 1200 K are presented in Figure 12 (other temperatures displayed similar results).

Viewing the results, a number of notable differences/features are apparent. First, overall short-range cluster distributions appear to follow a Boltzmann distribution, with the probability of an atom being attributed to a cluster of type $P_{\langle n_3, n_4, n_5, \ldots \rangle}$ being exponentially dependent on the mean potential energy of the central atom in the respective cluster $(P_{\langle n_3, n_4, n_5, \ldots \rangle} \propto exp(-\frac{\langle PE_{\langle n_3, n_4, n_5, \ldots \rangle}\rangle}{k_B T}))$. Interestingly, however, significantly greater scatter is evident for the CuZr system in comparison to the NiAl system. Moreover, Ni short-range cluster probabilities are heavily influenced by local energies, with significant energetic differences between the highest and lowest probability cluster types. While not conclusive, these differences support previous bonding considerations. Namely, the more short-range/covalent character of Ni–Al partial bonds and underlying mismatch between strain-stiffness

Mean Atomic Potential Energy and Voronoi Polyhedra Correlations
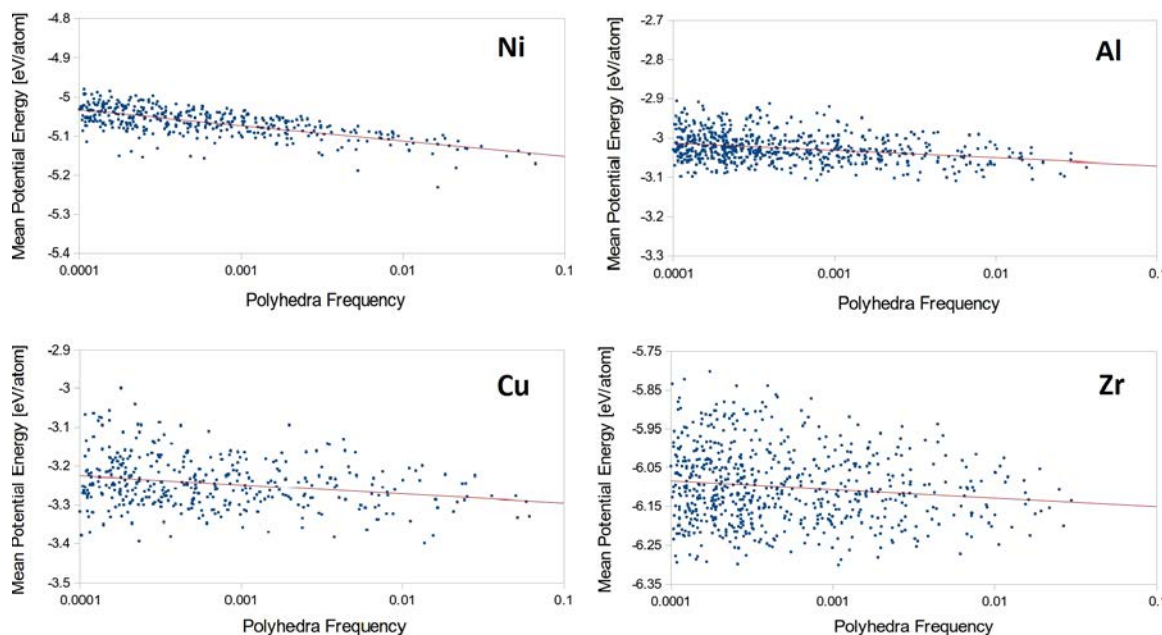

FIG. 12. Mean potential energies for central atoms in various sampled cluster types at 1200 K.

dependencies of Ni–Al, Ni–Ni, and Al–Al partial bonds are expected to largely constrain local bonding configurations, with certain local geometric configurations being highly favorable (low-energy) and others unfavorable (high-energy). On the other hand, longer-ranged interactions in the CuZr system would be expected to result in a higher relative influence of next-nearest-neighbor atomic configurations on local atomic potential energies. Moreover, the more metallic, non-directional bonding properties of the CuZr system would likely promote more collective rearrangement and relaxation behavior, further weakening the correlations between local cluster energies and probabilities.

IV. CONCLUSIONS

The computational search and discovery of high GFA alloys is currently limited to the use of GFA indicators which neglect to account for underlying differences in bonding properties or even the alloy class in question. Significant differences in the nature of atomic level bonding are reflected through more general differences in the degree and nature of short and medium-range ordering, energy landscape and structural relaxation properties, and ultimately the mechanisms through which crystal nucleation and growth occur. Consistent with these notions is the rapid crystal nucleation and growth rates observed in the $Ni_{50}Al_{50}$ system in comparison to $Cu_{50}Zr_{50}$, an apparently anomalous result which largely persists to be a source of confusion in the BMG community.

Thermodynamic analysis of NiAl and CuZr amorphous and B2 crystalline phases revealed lower phase stabilities for the NiAl system, most evident by NiAl's larger free energy difference at T_g and higher thermodynamic fragility. More significantly, the most marked indication of NiAl's lower thermal stability was identified upon analysis of fractional liquid-crystal density differences in the two systems. Results for the

NiAl system indicated fractional density differences ranging from 7%–11% along the quench, corresponding to values 2-3 times that of the CuZr system. The 10% volume change observed at T_m in the NiAl system marks a significant departure from the 0%–3% volume change characteristic of good glass forming systems.[32,33] These results suggest an inherently kinetic origin to NiAl's rapid crystallization rates. Surprisingly, the NiAl system was also identified to be the kinetically stronger system based on calculated strength and kinetic fragility parameters ($D^* = 2.07$ and 1.58, m = 61.4 and 75.5, respectively, for NiAl and CuZr), an unexpected result considering NiAl's lower GFA and thermodynamic fragility. These anomalies were further elucidated upon by investigations of Gruneisen parameter, bulk stiffness, and structural relaxation properties in the two systems. Large Gruneisen parameters and a sudden spike in bulk stiffness properties were identified near $1.3T_g$ in the NiAl amorphous phase, largely suggestive of the lower kinetic fragility being an artifact of underlying volume-strain and bond-stiffness dependencies. Importantly, these findings provide detailed evidence that the poor efficacy of the kinetic fragility parameter as a GFA indicator in alloy systems containing metalloid species in general is largely connected with the short-range/covalent character of TM–M bonding and underlying anharmonicity effects.

Mismatch between underlying strain-stiffness dependencies of Ni–Al, Ni–Ni, and Al–Al partial bonds is likely an inhibiting force preventing bulk structural relaxation to globally efficient packing structures in the high temperature NiAl melt. Subsequently, the high temperature NiAl melt exhibits high free volume content and high diffusive and viscous transport rates. As the system is cooled, associated volume contraction results in significantly increased interactions among previously "non-bonded" or poorly bonded Ni–Al atoms, translating to a sudden spike in bulk stiffness properties (bulk moduli), viscosities, and ultimately to a lower kinetic fragility.

In contrast, bonding in the CuZr system is longer-ranged, less directional, and highly metallic in character, translating to minimal short-range bonding constraints and promoting global structural relaxation (through more cooperative flow rearrangements) to lower free volume packing configurations. Structural evidence for the above included the more rapid decay of density correlations extending from the nearest-neighbor to next-nearest-neighbor coordination shells in the NiAl system, most notably apparent upon comparison of the ratio of first and second peak heights (summarized in Table IV) for Ni–Al and Cu–Zr pair-correlation functions (3.05 and 2.50, respectively). In conjunction with these observations, the high first peak intensities and large extent of bond-length shortening observed suggest significantly more pronounced Ni–Al nearest-neighbor level interactions. In contrast, longer-ranged next-nearest-neighbor interactions appear much more pronounced in the CuZr system, with strong and largely non-overlapping density correlations extending well into the 2nd, 3rd, and even 4th coordination shells indicative of more pronounced long-range ordering. Furthermore, Voronoi analysis revealed higher icosahedral ordering in the CuZr system (a signature of longer-ranged interactions and higher thermal stability of the amorphous phase) with higher fractions of $\langle 0,0,12,0 \rangle$, $\langle 0,2,8,2 \rangle$, and $\langle 0,2,8,1 \rangle$ clusters, as well as the presence of significantly more enhanced compositional short-range ordering. Analysis of chemical reordering along the quench was moreover suggestive of the strong bond strain-stiffness dependencies previously identified in the NiAl system having the additional negative side-effect of inhibiting compositional short-range ordering in the amorphous phase, a likely contributing factor to NiAl's lower GFA.

Considering the general correlations between glass forming ability and simple parameters such as the atomic size ratio, amorphous phase packing efficiency, and liquid fragility, the prospect of a rapid and robust compositional tuning approach reliant upon disordered phase properties alone may someday be realized. With that said, the findings of this paper highlight the critical importance of incorporating more complex alloy-specific information regarding the nature of bonding and ordering at the atomic level into such an approach. The results of this study therefore point towards the following conclusions and avenues for future research:

- Traditional free volume frameworks for diffusive motion and transport are likely to break down in alloys containing high concentrations of metalloid species due to the short-ranged/covalent nature of TM–M bonding.
- The poor efficacy of the fragility index as a GFA indicator in TM–M alloy systems is likely tied to underlying anharmonicity effects and bond strain-stiffness dependencies associated with the mismatch between short-ranged/covalent TM–M bonding and longer-ranged/metallic TM–TM bonding.
- Base BMG components should ideally be metallic so as to ensure longer-ranged interactions, more collective flow behavior, and enhanced medium-range ordering.
- Liquid-crystal density difference is the single most effective GFA indicator, however, proposed free volume theory based explanations provide at most a partial explanation for said efficacies. It is likely that in systems containing high fractions of metalloid species, a complete explanation requires consideration of induced stress fields at the liquid-crystal interface tied to underlying liquid-crystal density differences, bond-anharmonicity effects in the amorphous phase, and higher stiffness properties of the crystalline phase.
- A potential avenue for future research is the modification of common GFA indicators such as the fragility index to account for underlying bonding differences, potentially through the addition of terms accounting for anharmonicity, and bonding mismatch. In conjunction, cross-compositional analysis of (pseudo)Gruneisen parameters along the quenching domain may be worthwhile for the search of improved GFA indicators.

ACKNOWLEDGMENTS

[1]A. Inoue and A. Takeuchi, Acta Mater. **59**, 2243 (2011).
[2]J. Schroers, Phys. Today **66**(2), 32 (2013).
[3]A. Inoue and N. Nishiyama, MRS Bull. **32**, 651 (2007).
[4]W. Klement, R. H. Willens, and P. Duwez, Nature **187**, 869 (1960).
[5]A. Inoue, T. Zhang, and T. Masumoto, J. Non-Cryst. Solids **156-158**, 473 (1993).
[6]D. Turnbull, Contemp. Phys. **10**, 473 (1969).
[7]G. Ghosh, Acta Mater. **55**, 3347 (2007).
[8]A. Inoue, Acta Mater. **48**, 279 (1999).
[9]D. Miracle, W. Sanders, and O. N. Senkov, Philos. Mag. **83**, 2409 (2003).
[10]D. B. Miracle, Acta Mater. **54**, 4317 (2006).
[11]S. Mukherjee, J. Schroers, Z. Zhou, W. L. Johnson, and W. K. Rhim, Acta Mater. **52**, 3689 (2004).
[12]H. B. Yu, K. Samwer, W. H. Wang, and H. Y. Bai, Nat. Commun. **4**, 2204 (2013).
[13]Y. Li, Q. Guo, and J. A. Kalb, Science **322**, 1816 (2008).
[14]D.-H. Kang, H. Zhang, H. Yoo, H. H. Lee, S. Lee, G. W. Lee, H. Lou, X. Wang, Q. Cao, D. Zhang, and J. Jiang, Sci. Rep. **4**, 1 (2014).
[15]D. Turnbull, J. Chem. Phys. **52**, 3038 (1970).
[16]K. Russew, L. Stojanova, S. Yankova, E. Fazakas, and L. K. Varga, J. Phys.: Conf. Ser. **144**, 012094 (2009).
[17]C. Tang and P. Harrowell, Nat. Mater. **12**, 507 (2013).
[18]Z. W. Wu, M. Z. Li, W. H. Wang, and K. X. Liu, Nat. Commun. **6**, 6035 (2015).
[19]S. Plimpton, J. Comput. Phys. **117**, 1 (1995).
[20]M. Mendelev, M. Kramer, R. Ott, and D. Sordelet, Philos. Mag. **89**, 109 (2009).
[21]Y. Mishin, M. Mehl, and D. Papaconstantopoulos, Phys. Rev. B **65**, 1 (2002).
[22]S.-T. Lin, M. Blanco, and W. A. Goddard, J. Chem. Phys. **119**, 11792 (2003).
[23]P.-K. Lai, C.-M. Hsieh, and S.-T. Lin, Phys. Chem. Chem. Phys. **14**, 15206 (2012).
[24]Y. Zhang, N. Mattern, and J. Eckert, J. Appl. Phys. **110**, 093506 (2011).
[25]T. Chen, B. Smit, and A. T. Bell, J. Chem. Phys. **131**, 246101 (2009).
[26]P. J. Daivis and D. J. Evans, J. Chem. Phys. **100**, 541 (1994).
[27]C. H. Rycroft, Chaos **19**, 39 (2009).
[28]A. S. Roik, A. V. Anikeenko, and N. N. Medvedev, J. Struct. Chem. **54**, 332 (2013).
[29]J. C. Mauro, R. J. Loucks, A. K. Varshneya, and P. K. Gupta, Sci. Model. Simul. **15**, 241 (2008).

[30]C. A. Angell, J. Res. Natl. Inst. Stand. Technol. **102**, 171 (1997).

[31]K. Ito, C. T. Moynihan, and C. A. Angell, Nature **398**, 492 (1999).

[32]S. Mukherjee, Ph.D. thesis, California Institute of Technology, 2014.

[33]T. D. Shen, U. Harms, and R. B. Schwarz, Appl. Phys. Lett. **83**, 4512 (2003).

[34]B. Fultz, Prog. Mater. Sci. **55**, 247 (2010).

[35]C. Suryanarayana and A. Inoue, *Bulk Metallic Glasses* (Taylor & Francis Group, Boca Raton, FL, 2011), p. 124.

[36]R. Busch, JOM **52**, 39 (2000).

[37]T. Waniuk, R. Busch, A. Masuhr, and W. Johnson, Acta Mater. **46**, 5229 (1998).

[38]G. J. Fan, H. J. Fecht, and E. J. Lavernia, Appl. Phys. Lett. **84**, 487 (2004).

[39]C. Loken, D. Gruner, L. Groer, R. Peltier, N. Bunn, M. Craig, T. Henriques, J. Dempsey, C.-H. Yu, J. Chen, L. J. Dursi, J. Chong, S. Northrup, J. Pinto, N. Knecht, and R. V. Zon, J. Phys.: Conf. Ser. **256**, 012026 (2010).